# An investigation of mechanical-thermal coupling treatment on material properties, surface roughness, and cutting force of Inconel 718

Renjie Ji [a,b], Qian Zheng [a], Yonghong Liu [a], Suet To[b], Wai Sze Yip [b], Zelin Yang [a], Hui Jin [a], Haoyu Wang [a], Baoping Cai [a] , Weihai Cheng

[a] *College of Mechanical and Electronic Engineering, China University of Petroleum (East China), Qingdao 266580, Shandong, People's Republic of China*

[b] *State Key Laboratory in Ultra-precision Machining Technology, Department of Industrial and Systems Engineering, The Hong Kong Polytechnic University, Hong Kong, People's Republic of China*

# An investigation of mechanical-thermal coupling treatment on material properties, surface roughness, and cutting force of Inconel 718

It is common that Inconel 718 is difficult to cut, which limits its application unavoidably. In this study, the mechanical-thermal coupling (MTC) treatment method is applied to improve the machinability of Inconel 718. After MTC treatment on Inconel 718 surface, the severe plastic deformation is produced easily, and the grain is refined without new substance produced. Moreover, a theoretical and computational model taking account of the electric field, thermal field, and mechanical field simultaneously is proposed so as to predict the temperature and stress distributions during MTC treatment. Furthermore, the influence of peak current during MTC treatment on the material properties and the machinability of Inconel 718 in ultra-precision machining have been investigated. Results show that the workpiece surface grain size decreases and the thickness of the deformation layer increases with the increasing peak current. Moreover, with the appropriate MTC parameters, the small cutting force and the high cutting surface quality are obtained compared without MTC treatment, so MTC treatment can be used as an effective method for improving the machinability of Inconel 718 without deteriorating its base material performance, which is in favor of the application of the treated workpiece after machining.

Keywords: Mechanical-thermal coupling treatment, Inconel 718, Ultra-precision machining, Material property, Machining performance

Subject classification codes:

## Introduction

The nickel-based superalloy Inconel 718 has excellent corrosion resistance and superior mechanical property that is maintained at elevated temperature, so it has been put into use broadly in the aerospace industry. However, the high strength and the low coefficient of heat conduction result in the hard machinability of Inconel 718. The machinability of Inconel 718 is only 8–20% of steel, which makes it difficult for machining parts. Close tolerances and an outstanding surface finish are critical for the application of Inconel 718 [1]. Thus, any attempt to improve the machinability of such material is encouraged. Nowadays, coated cutting tools [2–6], air jet–assisted machining [7], laser-assisted machining (LAM) [8–12], and electrodischarge machining (EDM) [13–15] have been investigated to improve the machinability of Inconel 718. However, these methods have the following disadvantages. Firstly, the coated cutting tools have no appreciable benefit at the relatively high cutting speed [2, 3]. Secondly, the air jet–assisted machining needs a complex control system and shows high cost [7]. Thirdly, the heat transfer to the cutting tool, the lack of control on poor subsurface integrity, the high cost, and the large power consumption of high-powered lasers slow down the implementation of LAM [8, 11]. Fourthly, although the new EDM methods show the high material removal rate, the machined surface quality is poor, and the workpiece needs the subsequent precision machining [13, 15]. Ultrasonic vibration–assisted machining method uses the ultrasonic vibration energy to assist conventional machining, which is in favor of the machinability improvement of Inconel 718. Zhao et al. [16] studied single-point diamond turning Inconel 718 using the ultrasonic elliptical vibration cutting method. They found that the surface roughness generally decreased in magnitude. Li et al. [17] discussed how the ultrasonic vibration and peripheral speed of grinding wheel influenced the chip size and geometry in ultrasonic-assisted grinding (UAG) of Inconel 718. The results showed that the normal component force and tangential component force in UAG were both smaller than those in conventional grinding. Moreover, UAG could prospectively prevent the forming of shear chips and prefer the flow chips particularly at larger amplitude. It can be observed from the above literature survey that a complex ultrasonic system is needed during ultrasonicassisted machining, which shows high machining cost. Recently, an instantaneous high-energy input approach called electric pulse treatment has been put into use broadly, which can assist the deformation and control of the microstructure of metal materials. The movability of dislocations, vacancy diffusion, and atomic diffusion could be improved owing to coupling the thermal influence and the athermal influence of electrical pulse, which makes it ideal to assist the plastic deformation in rolling and drawing process. Some researchers have introduced electric pulse treatment to improve the metal machinability in recent years. Zhang et al. [18, 19] gone into the influence of electropulsing treatment on the changes of microstructure and ultra-precision machining of a rolled Mg-9Al-1Zn alloy. The results revealed that the cutting force was decreased and the surface quality was improved after electropulsing treatment, meaning the improvement of the AZ91 alloy machinability. Lou and Wu [20] applied electric pulse treatment to alter the Ti6Al4V properties and the Ti6Al4V machinability in ultra-precision machining. They found that the variation of mechanical properties enhanced the Ti6Al4V machinability with the cutting force decrease and the machining quality improvement. Wang et al. [21] introduced electropulsing into turning AISI 304 stainless steel. The consequences revealed that the primary cutting force, the microhardness, and the axial machined surface roughness all decreased under the proper parameters of electropulsing treatment. Although the metal machinability has been improved by introducing electric pulse treatment according to the above literature, the overall property of the metal material is easily changed because the whole metal material is performed by electric pulse treatment simultaneously, which is not appropriate for the application of the treated material after machining. The mechanical-thermal coupling (MTC) treatment method has been proposed by our previous research, and gradient nanostructure layer is prepared efficiently on the commercial pure copper surface [22, 23]. In this study, the MTC treatment method, which can only change the surface property but not deteriorate the base material performance of Inconel 718, is applied to improve the ultraprecision machinability of Inconel 718. Moreover, a theoretical and computational model to predict the temperature and stress distributions during MTC treatment has been proposed, and the effect of peak current on material properties and ultra-precision machining performance of Inconel 718 has been investigated.

## Principle and experiment details for MTC treatment

### *Principle for MTC treatment*

The schematic of MTC principle is displayed in Fig. 1a. It can be observed from the figure that during MTC, the workpiece surface is acted by both the force and the heat from tool impacting. The thermal impacting can raise the temperature at the touch point to the expected value rapidly, which can make the material plasticity at the touch point increase; the plastic zone is generated rapidly; and then the ultrasonicfrequency mechanical impacting can cause the severe plastic deformation at the plastic zone, so the grain can be refined at the plastic region. As shown in Fig. 1b, the mechanical force consists of two parts: the preload pressure from the air pressure and the impact force from the ultrasonic generator, and the heat is produced by the high-instantaneous energy-density pulse current from the pulse power supply during MTC treatment. Figure 1c depicts the developed experimental device for MTC treatment. As shown in the figure, the workpiece rotates along its axial direction with the velocity $V_1$. Meanwhile, the treatment tool acts on the end face of the workpiece and slides along the end face with the velocity $V_2$. As the tool tip slides from the end to the other end of the end face, the workpiece surface is considered being treated by one pass. During MTC, the workpiece and the tool are linked to the negative pole and the positive pole of the pulse generator, respectively. In order to dissipate the generated heat quickly, the cooling medium is flushed to the touch point between the tool and the workpiece using a jet nozzle at room temperature. Moreover, the microthermal impacting by the electric pulse and the micromechanical ultrasonic impacting act on the workpiece surface simultaneously. Meanwhile, at the touch point, the high peak pulse current causes the electron in the material to move along the electric field quickly, and the great electron wind force is generated; as a consequence, the deformation resistance decreases greatly, and the severe plastic deformation occurs, which can refine the grain on the metal surface easily after sufficient pass treatment. There are two reasons for the improvement of machining performance during MTC. Firstly, according to Astakhov [24], the energy spent in actual cutting is much smaller than it should be because a certain cold working in the layer is achieved, which leads to the process machinability being improved. In this paper, the principle of the MTC treatment is shown in Fig. 1. It can be seen from Fig. 1a that the force and the heat act on the surface of workpiece at the same time during treatment. The force acting on the surface of the workpiece is similar with the “cold working” mentioned above. Secondly, the thermal impacting in Fig. 1a can raise the temperature at the touch point to the expected value rapidly, which can make the plasticity of the touch point increase; the plastic zone is generated rapidly; and then the ultrasonic-frequency mechanical impacting can cause the severe plastic deformation at the plastic zone. As a result, the thermal acting on the workpiece can further enhance the effect of cold working, which makes the surface plastic deformation in cold working generated more easily. Consequently, the machining performance is further improved.

***Experiment details for MTC treatment of Inconel 718***

In this investigation, Inconel 718 nickel–based superalloy was taken as the workpiece, its microstructure is shown in Fig. 2, and its chemical composition is shown in Fig. 3. The average grain diameter of Inconel 718 was 9.55 μm (Fig. 2). The Inconel 718 specimen was a cylinder with the diameter of 20 mm and the length of 300 mm. An MG18 hard alloy cylinder with a hemispherical tip was used as the treatment tool, and the diameter of the cylinder was 6 mm. During MTC, $V_1$ was 250 rpm; $V_2$ was 5 mm/min; the frequency of the ultrasonic vibration was 26 kHz; the amplitude of the ultrasonic vibration was 10 μm; the frequency of electric pulse was 1000 Hz; the peak currents of electric pulse were 0 A, 600 A, and 1000 A, respectively; and each specimen was treated 12 passes with the same condition. It is necessary to make the ultrasonic vibration tool stay in good contact with the workpiece, so the static force was set to 600 N.

***Test details for treated specimens***

To investigate the effect of MTC parameter on Inconel 718 properties, structural characterization and microhardness test were performed. The details are as follows: The sample preparation for metallographic examination followed the ordinary route of cutting, mounting, polishing, and etching with aqua regia at room temperature, and then the metallographic structure of the treated sample was observed with a metallurgic microscope (DM2500M; Leica, Germany). For analyzing the untreated and the treated workpiece, a thermal field emission scanning electron microscope (JEOL JSM-7001F, JEOL Ltd.) with an electron backscatter diffraction (EBSD) analysis apparatus (TSL Incorporated) was used. Structural characteristics of the treated surface were obtained by an X-ray diffraction (XRD) (X'Pert PRO MPD) with a CuKα radiation; moreover, the acceleration voltage was 40 kV, and the applied current was 40 mA during the XRD test. Transmission electron microscopy (TEM) (Tecnai G2 F20 S-TWIN) was applied to analyze the grain size of the treated surface. Moreover, the voltage was set as 200 kV, and a focused ion beam (FIB) (Helios NanoLab 600i) was used to prepare the observed sample during the TEM test. The microhardness of the workpiece surface was measured using a digital microhardness tester (TIME6610M; Beijing TIME High Technology Ltd., China) with a diamond Vickers indenter under a load of 0.98 N for 15 s. It is worth mentioning that each specimen was tested five times under the same testing conditions. As a result, the observed microhardness and the grain size of the treated surface were both obtained by averaging five experimental measurements.

## Modeling for MTC treatment

### *Modeling of the electrical field during MTC treatment*

Because the workpiece and the treatment tool are both axisymmetric and the magnetic field is so small that its effect can be considered negligible, the electric field can be written as the following steady equation [25]:

$$\frac{1}{r}\frac{\partial}{\partial r}\left(r\varepsilon\frac{\partial V}{\partial r}\right)+\frac{\partial}{\partial z}\left(\varepsilon\frac{\partial V}{\partial z}\right)=0 \qquad (1)$$

where ε is the electrical conductivity of material. At the top surface of the tool, the electric current was applied evenly, which satisfies the following condition:

$$\int\varepsilon\left(\frac{\partial V}{\partial n}\right)ds=i(t) \qquad (2)$$

where i(t) is the pulse current during MTC treatment. Moreover, at the other surfaces and symmetric axis, the potential gradient is 0.

### *Modeling of the thermal field during MTC treatment*

The heat transferred to the workpiece in unit time can be calculated according to Joule's law as follows:

$$q=\eta_1 i^2(t)R \qquad (3)$$

where $\eta_1$ is the heat distribution coefficient transferred to the workpiece and R is the total resistance, which is composed of the workpiece resistance, the contact resistance at the touch point, and the tool resistance. During MTC treatment, the heat convection between the workpiece and the cooling medium occurs, so some heat will be lost, and the dissipation heat in unit time can be calculated as follows [25]:

$$q_{loss} = k_1 A(\eta_3 T - T_0) \tag{4}$$

where $k_1$ is the convective thermal conductivity, A is the heat dissipation region, $\eta_3$ is the temperature distribution coefficient on the workpiece surface, T is the temperature on the workpiece surface, and $T_0$ is the environment temperature. Moreover, the unsteady heat conduction formula in plane is as follows [25]:

$$pc\frac{\partial T}{\partial t} = \frac{\partial}{\partial y}\left(k\frac{\partial T}{\partial y}\right) + \frac{\partial}{\partial x}\left(k\frac{\partial T}{\partial x}\right) + q \tag{5}$$

where ρ is the workpiece density, c is the specific heat of the workpiece, k is the thermal conductivity of the workpiece, and q is the net heat transferred to the workpiece in unit time. Substituting Eqs. (3) and (4) into Eq. (5) and considering the mechanical force transferred to the workpiece, the temperature distribution on the workpiece surface can be expressed as follows:

$$pc\frac{\partial T}{\partial t} = \frac{\partial}{\partial y}\left(k\frac{\partial T}{\partial y}\right) + \frac{\partial}{\partial x}\left(k\frac{\partial T}{\partial x}\right) + \eta_1 i^2(t)R + \eta_2 P - k_1 A(\eta_3 T - T_0) \quad (6)$$

where $\eta_2$ is the heat removal coefficient of the workpiece and P is the mechanical power during MTC treatment.

***Modeling of the stress field during MTC treatment***

During MTC treatment, the displacement of the mechanical ultrasonic vibration can be expressed as follows:

$$l = Lcos(2\pi f_U t) \quad (7)$$

where L is the displacement amplitude of the mechanical ultrasonic vibration and $f_U$ is the frequency of the mechanical ultrasonic vibration. During the mechanical ultrasonic vibration, the pressure of the ultrasonic vibration tool acted on the workpiece surface can be expressed as follows:

$$F_U = F_0 - Msin(2\pi f_U t + \pi/2) \quad (8)$$

where $F_0$ is the preload pressure and M is the impact force amplitude of the mechanical ultrasonic vibration. The pit pressed by the mechanical ultrasonic vibration tool is shown in Fig. 4 where $R_0$ is the radius of the ultrasonic vibration tool, so the projection area of the pit on the workpiece can be calculated as follows:

$$S = \pi\left[R_0^2 - (R_0 - 1)^2\right] = 2\pi R_0 L cos(2\pi f_U t) - \pi L^2 cos^2(2\pi f_U t) \quad (9)$$

The stress at the touch point by the mechanical force can be calculated as follows:

$$\sigma_U = \frac{F_U}{S} = \frac{F_0 – Msin(2\pi f_U t + \pi/2)}{2\pi R_0 L cos(2\pi f_U t) - \pi L^2 (2\pi f_U t)} \quad (10)$$

During MTC, the thermal stress can also be generated by the pulse current heat, and the thermal stress along the vertical direction can be expressed as follows:

$$\sigma_H = \frac{E}{1-\mu^2}\left(\frac{\partial v}{\partial y} + \mu \frac{\partial u}{\partial x}\right) - \frac{E\alpha T}{1-\mu} \quad (11)$$

where E is Young’s modulus of the workpiece, μ is Poisson’s ratio of the workpiece, α is the linear expansion coefficient of the workpiece, and u and v can be expressed as follows:

$$\left.\begin{aligned} \frac{\partial^2 u}{\partial x^2} + \frac{1-\mu}{2}\cdot\frac{\partial^2 u}{\partial y^2} + \frac{1+\mu}{2}\cdot\frac{\partial^2 v}{\partial x \partial y} - (1+\mu)\alpha\frac{\partial T}{\partial x} = 0 \\ \frac{\partial^2 v}{\partial y^2} + \frac{1-\mu}{2}\cdot\frac{\partial^2 v}{\partial x^2} + \frac{1+\mu}{2}\cdot\frac{\partial^2 u}{\partial x \partial y} - (1+\mu)\alpha\frac{\partial T}{\partial y} = 0 \end{aligned}\right\} \quad (12)$$

The boundary conditions are as follows:

$$\left.\begin{aligned} l\left(\frac{\partial u}{\partial x}+\mu\frac{\partial v}{\partial y}\right)+m\frac{1-\mu}{2}\left(\frac{\partial u}{\partial y}+\frac{\partial v}{\partial x}\right)_s &= l(1+\mu)\alpha T \\ m\left(\frac{\partial v}{\partial y}+\mu\frac{\partial u}{\partial x}\right)+l\frac{1-\mu}{2}\left(\frac{\partial v}{\partial x}+\frac{\partial u}{\partial y}\right)_s &= m(1+\mu)\alpha T \end{aligned}\right\} \quad (13)$$

where l and m are the direction cosine, and during MTC, they are as follows:

$$\begin{cases} l=1 \\ m=0 \end{cases}, \begin{cases} l=0 \\ m=1 \end{cases}, \begin{cases} l=-1 \\ m=0 \end{cases} \quad (14)$$

Considering the mechanical force and the pulse current heat, the total stress in the workpiece during MTC can be calculated as follows:

$$\sigma=\sigma_U+\sigma_H=\frac{F_0\text{–}Msin(2\pi f_U t+\pi/2)}{2\pi R_0 Lcos(2\pi f_U t)-L^2cos^2(2\pi f_U t)} + \frac{E}{1-\mu^2}\left(\frac{\partial v}{\partial y}+\mu\frac{\partial u}{\partial x}\right)-\frac{E\alpha T}{1-\mu} \quad (15)$$

***The FEM simulation of MTC treatment***

A computational model was developed according to Eqs. 6 and 15 on the basis of the finite element ANSYS software, and the temperature field and the strain field were calculated during MTC. Tables 1 and 2 list partial essential parameters of the treatment tool and the workpiece applied in the model ANSYS. The simulation model is shown in Fig. 5. The boundary conditions of the simulation were as follows:

1. The fixed constraints were applied on both sides of the vibrating head and on both sides and bottom of the workpiece. The bottom of the vibrating head was always in contact with the top of the workpiece.

2. A force of 600 þ 250sin π 2  105t  N was applied to the top of the vibrating head.

3. The pulse current with a peak current of 0 A, 600 A, and 1000 Awas evenly applied to the top of the vibrating head and the bottom of the workpiece.

4. The convection coefficient of the water-based fluid was 1200 W/m2 /°C.

5. The temperature of finite element simulation was 22 °C.

**Experiment details for ultra-precision machining of Inconel 718**

In this research, all the cutting experiments for treated Inconel 718 were conducted on a four-axis ultra-precision machine (Nanotech 350 UPL; Moore, USA), as shown in Fig. 6, under the following cutting conditions: cutting depth of 4 μm, feeding speed of 4 mm/min, and spindle speed of 1500 rpm. The parameters of cubic boron nitride (CBN) cutting tool are as follows: tool nose radius of 0.610 mm, tool rake angle of 0°, and front clearance angle of 15°, and the cutting environment was "lubricant compressed air + mineral oil to form a mist." In addition, the granularity of the CBN cutting tool was fine, the concentration of the cutting tool was 80%, and the binder was Co. The output pressure of cool air in minimal quantity lubrication (MQL) device was 0.225 MPa, the temperature of MQL was − 5 °C, the type of lubricating oil was BesluxBescut 173, the viscosity of lubricating oil was 100 $mm^2$ /s, the output oil volume was 10 ml/h, and the nozzle pointed in the direction of feed. During the cutting experiments, a dynamometer (Kistler 9252A) was applied to detect the cutting force, and the signal of cutting force was recorded with a sample frequency of 100 kHz. To investigate the effect of peak current on the machined surface, the optical profiling system (WYKONT8000) was applied to examine the micromorphology of the machined surface with different peak currents. The microstructure of the cutting chips was examined with an electron probe micro-analyzer (EPMA JEOL JXA-8230, Japan).

## Result and discussion

### ***Influence of MTC treatment on the material properties of Inconel 718***

Figures 7 and 8 show the microstructure, the microhardness, and the average grain size of the treated Inconel 718 surface with different peak currents, respectively. It can be observed from Fig. 8a that the hardness of the treated surface increases after MTC treatment. Meanwhile, the hardness from the surface to the matrix gradually decreases. Besides, the thickness of the hardened layer increases with the increase of the current. At the same depth, the hardness increases with the increase of peak current. It can be seen from Figs. 7a, c, and e and 8 that the treated surface grain is refined, and the microhardness increases compared with the matrix. Moreover, as the peak current increases, the grain becomes small and uniform, and the microhardness increases gradually. It is worth mentioning that with the peak current of 1000 A during MTC treatment, the average surface grain size (36.8 nm) is decreased by 99.6%, and the microhardness (615.3 HV) is increased by 50.4% compared with the matrix. The phenomena can be explained as follows: When the peak current is 0 A, only the micromechanical shock by the ultrasonic apparatus impacts the workpiece surface, a certain plastic deformation takes place at the surface, and the original grain is refined in the plastic deformation layer. As the peak current is bigger than 0 A, the microthermal shock by electric pulse impacts the workpiece surface as well, which results in the high temperature distribution and the high temperature gradient at the touch point (Fig. 9a), and then the high thermal stress is generated. Combining the effect of the continuous ultrasonic vibration, the high stress is produced at the touch point. It can be observed from Fig. 9b that the equivalent stress at the touch point is about 1322.55 MPa, which far exceeds the yield strength of Inconel 718 (510 MPa). Meanwhile, at the touch point, the high-instantaneous energy-density pulse current can cause the electron in the material to move along the electric field quickly, which may cause the deformation resistance to decrease tremendously and the plasticity to be enhanced greatly at the touch point as well. Therefore, the severe plastic deformation takes place, and a great number of dislocations are generated in the treated surface. The dislocation wall and the dislocation tangle are formed by the slip, accumulation, interaction, and rearrangement of the dislocations (Fig. 10), and they will develop into the high-angle grain boundary which can split the original large grain into many small ones. Moreover, as the peak current decreases, the temperature distribution and the equivalent stress at the touch point decrease (Fig. 9), so the severe plastic deformation decreases, the grain size increases, and the microhardness decreases. It can also be seen from Fig. 7b, d, and fthat the plastic flow occurs at the treated surface, and the surface grain is elongated simultaneously. Moreover, the plastic deformation at the treated surface decreases gradually from the top surface to the base of the workpiece, and the thickness of the deformation layer increases with the increasing peak current. The phenomena can be explained as follows: During MTC treatment, the force is tangent to the treated surface on account of the movement of tool tip, and as a result, the grains on the surface are elongated and almost parallel to the treated surface. Moreover, the force from ultrasonic and the heat from electric pulse both decrease as the depth of the treated surface increases. Thus, the plastic flow occurs at the treated surface, and the severe plastic deformation decreases gradually as the depth of the treated surface increases. Furthermore, as the peak current increases, the thermal impacting from the electric pulse increases and the affected zone is intensified in depth, so the thicknesses of the deformation layer increases. In order to detect whether the phase change happens during MTC treatment, the XRD analysis has been carried out on the workpiece surface with different peak currents, and the result is displayed in Fig. 11. It is observed from the figure that only broadening of the diffraction peak happens and no new diffraction peak appears after the treatment, which means that only the workpiece surface grain is refined and no other substance is generated during the treatment. This finding suggests that it is reasonable to ignore the tool contamination, particularly on the top surface. The reason for this phenomenon may be that the short touch time and the cooling temperature restrain the interdiffusion of elements between the tool and the treated material. Figure 12 illustrates the pole figure of the Inconel 718 section from the top surface of 70 μm treated with different peak currents. It can be observed from this figure that there is no obvious texture generated on the treated workpiece surface in contrast with the initial workpiece surface, although the grain is refined. That is to say the workpiece maintains isotropic after the treatment.

***Influence of MTC treatment on ultra-precision machining performance of Inconel 718***

In order to study the effect of the MTC parameters on the machinability of Inconel 718 during ultra-precision machining, the matrix without MTC treatment is also machined in the cutting experiment. The surface topography of Inconel 718 treated with different peak currents is shown in Fig. 13. It can be observed from this figure that the surface roughness of any treated Inconel 718 is smaller than that of the matrix, and the surface roughness decreases with the increasing peak current. The reasons for this phenomenon are as follows: The grain size of the treated Inconel 718 surface is smaller than that of the matrix, and the grain size decreases with the increasing peak current (Fig. 7). As the peak current increases, the Inconel 718 surface defect decreases, the surface residual stress of Inconel 718 decreases on account of the high temperature recrystallization, and the coordination of the inhomogeneous deformation among the grains during machining is improved [26], so the surface roughness decreases with the increasing peak current. The cutting force of Inconel 718 treated with different peak currents is shown in Fig. 14. As calculated from Fig. 14, the average cutting force with matrix and Inconel 718 treated with 0 A, 600 A, and 1000 A is 7.43 N, 7.31 N, 4.85 N, and 6.92 N, respectively. It can be seen that the surface hardness increases, the cutting force decreases first and then increases, and the surface quality becomes better as the grain size decreases. The detailed analyses are as follows.

***The reasons why the surface hardness increases***

According to the relation proposed by Armstrong [27]:

$$H = H_0 + k_H l^{-1/2} \tag{16}$$

where H is the hardness, $H_0$ and $k_H$ are the experimental constants, and l is the average grain diameter. It can be seen from Eq. (16) that the hardness (H) increases when the average grain diameter (l) decreases.

***The reasons why the cutting force decreases***

When the grain size decreases from 9550 to 150.5 nm, the surface hardness increases, the cutting force decreases, and the surface roughness decreases. The reasons why the cutting force decreases are as follows: In the direction of the shear force, the machined materials in the primary deformation zone are squeezed out. The cutting materials can be split from the workpiece and become chips when the plastic deformation reaches to the limit [28]. Moreover, the intergranular tensile stress occurs due to the inhomogeneous deformation among the grains during machining [26]. As the grain size is big, the coordination of the inhomogeneous deformation is bad, and the brittle intergranular fracture occurs easily, which induces the high cutting force and the serrated chip with severe cracks. However, as the grain size decreases, the dislocation sliding distance is shortened effectively, the local deformation and the stress distribution become uniform, and the stress concentration is reduced, so the cutting force decreases and the continuous chips are obtained, which means that the cutting process becomes more stable on account of MTC treatment.

***The reasons why the cutting force increases***

When the average grain size decreases from 150.5 to 36.8 nm (minimum), the hardness increases, the cutting force increases, and the surface quality is improved. The reasons why the cutting force increases are as follows: The stress acting on the boundary $\tau^{GB}_i$ is given by the following expression [29]:

$$\tau_i^{GB} = \pi D_{GB} \tau^2 \frac{k}{Gb} \tag{17}$$

where $D_{GB}$ is the grain size, τ is the applied stress, G is the shear modulus, b is the Burgers vector, and k is a constant equal to (1 − υ), where υ is Poisson's ratio. G and b are the constants related to the material.

In addition, the $\tau^{GB}_i$ can also be given by the following expression [29]:

$$\tau_i^{GB} = \left(\frac{k_1}{M}\right)^2 \left(\frac{\pi 0.85}{Gb}\right) \tag{18}$$

where M is the Taylor factor and $k_1$ is a constant.

It can be seen from Eq. (18) that $\tau^{GB}_i$ is a constant for a given material.

Additionally, it can be obtained from Eq. (17)

$$\tau^2 = \tau_i^{GB} \frac{Gb}{k\pi} \frac{1}{D_{GB}} \tag{19}$$

In Eq. (19), ($\tau_i^{GB} \frac{Gb}{k\pi}$) is a constant related to the material. As a result, a constant called Ψ is defined as follows: $\Psi = \tau_i^{GB} \frac{Gb}{k\pi}$. Introducing the constant Ψ, Eq. (19) is obtained

$$\tau^2 = \Psi \frac{1}{D_{GB}} \tag{20}$$

The applied stress (τ) is given by the following expression [30]:

$$\tau = \frac{F_t \cos\phi - F_f \sin\phi}{A_s} \tag{21}$$

where $F_t$ is the tangential force, $F_f$ is the feed force, As is the shear plane area, and ϕ is the shear angle. The shear angle can be determined experimentally from measured cutting force signals and the tool geometry [31]. The shear plane area ($A_s$) is given by the following expression [30]:

$$A_s = l_{AB}\frac{d_c}{\sin\phi} \tag{22}$$

where dc is the cutting depth. The average length ($l_{AB}$) is measured from the serrated chips after diamond turning [30].

It can be obtained from Fig. 15

$$F_t = F\cos(\beta_a - \alpha_r) \tag{23}$$

$$F_f = F\sin(\beta_a - \alpha_r) \tag{24}$$

where $\beta_a$ is the average friction angle, αr is rake angle, and F is the resultant force. As can be seen from Fig. 15, the angle between the resultant force (F) and shear plane is given by the following expression: Y = ϕ + βa − αr, and as a result

$$\beta_a - \alpha_r = \Upsilon - \phi \tag{25}$$

where Y is also the angle between the resultant force (F) and the shear force ($F_s$). Besides, it should be noted that Y varies over a small range depending on the material and Y is approximately equal to 45° [32]. Substituting Eqs. (22), (23), (24), and (25) into Eq. (21), the applied stress can be expressed as follows:

$$\tau = \frac{F\cos\Upsilon\sin\phi}{l_{AB}d_c} \tag{26}$$

Substituting Eq. (26) into Eq. (20), the cutting force can be expressed as follows:

$$F^2 = \left(\frac{l_{AB} d_c}{\cos\Upsilon \sin\phi}\right)^2 \Psi \frac{1}{D_{GB}} \tag{27}$$

It can be observed from Eq. (27) that the cutting force (F) increases when the grain size ($D_{GB}$) decreases.

It can be seen from the above analysis that the increase of surface hardness is an inevitable result of grain refinement. But within the grain size range of 150.5~9550 nm, the refinement of grains reduces the cutting force and improves the surface quality, which improves the machinability of Inconel 718.

In conclusion, the appropriate MTC-induced grain refinement of Inconel 718 is in favor of the improvement of its machinability during ultra-precision machining.

**Conclusion**

In this study, the ultrasonic-frequency MTC treatment method is applied. Moreover, a theoretical and computational model to predict the temperature and stress distributions during MTC treatment has been proposed, and the effect of peak current on material properties and ultra-precision machining performance of Inconel 718 has been studied. The conclusions drawn are as follows:

1. Inconel 718 surface is impacted by the micromechanical ultrasonic shock; the microthermal shock caused by the electric pulse at the same time during MTC treatment, the high temperature distribution, and the high stress distribution are

produced at the touch point; and the severe plastic deformation occurs easily, so the grain is refined easily after MTC treatment.

2. The workpiece surface grain size decreases, and the thicknesses of the deformation layer increases with the increasing peak current. Furthermore, the workpiece surface maintains isotropic after MTC treatment.

3. The machined surface roughness of the treated Inconel 718 is smaller than that of the matrix, and the surface roughness decreases with the increasing peak current. Moreover, the cutting force of the treated Inconel 718 is smaller than that of the matrix in this investigation.

4. MTC treatment can only change the surface property of Inconel 718, and the machining performance of Inconel 718 in ultra-precision machining can be improved by the appropriate MTC-induced grain refinement, and as a result, MTC treatment is a useful way of decreasing the cutting force and enhancing the cutting surface quality, which is in favor of its application.

**Completing Interests**

The authors declare that they have no competing interests.

**Acknowledgments**

This work was supported by the National Natural Science Foundation of China (Grant No. 51675535), the Major Research Project of Shandong Province (Grant No. 2019GGX104068), the Key Pre-Research Foundation of Military Equipment of China (Grant No. 6140923030702), and the Fundamental Research Funds for Central Universities (Grant No. 17CX02058).

**References**

1. Shokrani A, Newman ST (2018) Hybrid cooling and lubricating technology for CNC milling of Inconel 718 nickel alloy. Procedia CIRP 77:215–218

2. Bushlya V, Zhou J, Ståhl JE (2012) Effect of cutting conditions on machinability of superalloy Inconel 718 during high speed turning with coated and uncoated PCBN tools. Procedia CIRP 3:370–375

3. Soo SL, Khan SA, Aspinwall DK, Harden P, Mantle AL, Kappmeyer G, Pearson D, Saoubi RM (2016) High speed turning of Inconel 718 using PVD-coated PCBN tools. CIRP Ann Manuf Tec 65:89–92

4. Criado V, Díaz-Álvarez J, Luis Cantero J, Miguélez MH (2018) Study of the performance of PCBN and carbide tools in finishing machining of Inconel 718 with cutting fluid at conventional pressures. Procedia CIRP 77:634–637

5. Zhou J, Avdovic P, Ståhl JE (2012) Study of surface quality in high speed turning of Inconel 718 with uncoated and coated CBN tools. Int J Adv Manuf Technol 58(1–4):141–151

6. Grguraš D, Kern M, Pušavec F (2018) Suitability of the full body ceramic end milling tools for high speed machining of nickel based alloy Inconel 718. Procedia CIRP 77:630–633

7. Obikawa T, Yamaguchi M, Funai K, Kamata Y, Yamada S (2012) Air jet assisted machining of nickel-base superalloy. Int J Mach Tools Manuf 61:20–26

8. Navas VG, Arriola I, Gonzalo O, Leunda J (2013) Mechanisms involved in the improvement of Inconel 718 machinability by laser assisted machining (LAM). Int J Mach Tools Manuf 74:19–28

9. Anderson M, Patwa R, Shin YC (2006) Laser-assisted machining of Inconel 718 with an economic analysis. Int J Mach Tools Manuf 46:1879–1891

10. Navas VGA, Arriola I, Gonzalo O, Leunda J (2013) Mechanisms involved in the improvement of Inconel 718 machinability by laser assisted machining (LAM). Int J Mach Tools Manuf 77:19–28

11. Venkatesan K (2017) The study on force, surface integrity, tool life and chip on laser assisted machining of inconel 718 using Nd:YAG laser source. J Adv Res 8:407–423

12. Venkatesan K, Ramanujam R, Kuppan P (2016) Parametric modeling and optimization of laser scanning parameters during laser assisted machining of Inconel 718. Opt Laser Technol 78:10–18

13. Atzeni E, Bassoli E, Gatto A, Iuliano L, Minetola P, Salmi A (2015) Surface and sub surface evaluation in coated-wire electrical discharge machining (WEDM) of Inconel alloy 718. Procedia CIRP 33:388–393

14. Beri N, Maheshwari S, Sharma C, Kumar A (2014) Surface quality modification using powder metallurgy processed CuW electrode during electric discharge machining of Inconel 718. Procedia Mater Sci 5:2629–2634

15. Ahmed A, Fardin A, Tanjilul M, Wong YS, Rahman M, Senthil Kumar A (2018) A comparative study on the modelling of EDM and hybrid electrical

discharge and arc machining considering latent heat and temperature-dependent properties of Inconel 718. Int J Adv Manuf Technol 94:2729–2737

16. Zhao H, Li S, Zou P, Kang D (2017) Process modeling study of the ultrasonic elliptical vibration cutting of Inconel 718. Int J Adv Manuf Technol 92:2055–2068

17. Li S, Wu Y, Nomura M (2016) Effect of grinding wheel ultrasonic vibration on chip formation in surface grinding of Inconel 718. Int J Adv Manuf Technol 86:1113–1125

18. Zhang D, To S, Zhu Y, Wang H, Tang G (2012) Electropulsinginduced phase transformations and their effects on the single point diamond turning of a tempered alloy AZ91. Int J Mater Res 103: 1205–1209

19. Zhang D, To S, Zhu Y, Wang H, Tang G (2012) Static electropulsing-induced microstructural changes and their effect on the ultra-precision machining of cold-rolled AZ91 alloy. Metall Mater Trans A 43:1341–1346

20. Lou Y, Wu H (2017) Improving machinability of titanium alloy by electro-pulsing treatment in ultra-precision machining. Int J Adv Manuf Technol 93:2299–2304

21. Wang H, Chen L, Liu D, Song G, Tang G (2015) Study on electropulsing assisted turning process for AISI 304 stainless steel. Mater Sci Technol 31(13):1564–1571

22. Ji R, Yang Z, Jin H, Liu Y, Wang H, Zheng C, Cheng W, Cai B, Li X (2019) Surface nanocrystallization and enhanced surface mechanical properties of nickel-based superalloy by coupled electric pulse and ultrasonic treatment. Surf Coat Technol. https://doi.org/10. 1016/j.surfcoat.2019.07.037

23. Ji R, Liu Y, To S, Jin H, Yip W, Yang Z, Zheng C, Cai B (2018) Efficient fabrication of gradient nanostructure layer on surface of commercial pure copper by coupling electric pulse and ultrasonics treatment. J Alloys Compd 764:51–61

24. Astakhov VP (2014) Chapter 1. Machinability: existing and advanced concepts. In: Davim JP (ed) Machinability of advanced materials. Waley, London, pp 1–56

25. Shen J, Zhang Y, Lai X, Wang PC (2011) Modeling of resistance spot welding of multiple stacks of steel sheets. Mater Design 32: 550–560

26. Hou J, Zhao Z, Yan G, Liu L (2007) The changing of machinability of superalloys after grain refinement. Met Funct Mater 14:11–14

27. Armstrong RW (1970) The influence of polycrystal grain size on several mechanical properties of materials. Metall Mater Trans A 1: 1169–1176

28. Chen X, Xiao J, Zhu Y, Tian R, Shu X, Xu J (2017) Micromachinability of bulk metallic glass in ultra-precision cutting. Mater Design 136:1–12

29. Hansen N (2005) Boundary strengthening in undeformed and deformed polycrystals. Mat Sci Eng A-Struct 409:39–45

30. Zhao Z, To S, Wang J (2019) Effects of grains and twins on deformation of commercial pure titanium in ultraprecision diamond turning. J Mater Process Technol 271:10–22

31. Berezvai S, Molnar TG, Bachrathy D, Stepan G (2018) Experimental investigation of the shear angle variation during orthogonal cutting. Materials Today: Proceedings 5:26495–26500

32. Junhai Liu, Modeling method and simulation research of cutting force, Diss. Xi’an University of Technology (2009)

Table 1 Material properties of the workpiece and the treatment tool

| | Inconel 718 nickel–based superalloy | Cemented carbide |
| --- | --- | --- |
| Density (kg/m$^3$) | 8.19 x $10^3$ | 12.90 x $10^3$ |
| Thermal expansion coefficient (K$^{-1}$) | 1.3 x $10^{-5}$ | 6 x $10^{-6}$ |
| Heat conductivity (W/m K) | 11.4 | 110 |
| Specific heat (J/kg K) | 435 | 950 |
| Yield strength (MPa) | 510 | 946 |

Table 2 Mechanical properties of the Inconel 718 nickel–based superalloy

| Temperature (K) | Elastic modulus (GPa) | Tangent modulus (GPa) | Poisson's ratio |
| --- | --- | --- | --- |
| 294 | 211 | 21.1 | 0.29 |
| 421 | 203.7 | 20.37 | 0.28 |
| 533 | 197.2 | 19.72 | 0.27 |
| 644 | 190.6 | 19.06 | 0.27 |
| 810 | 180.4 | 18.04 | 0.27 |
| 921 | 172.4 | 17.25 | 0.28 |
| 1088 | 155 | 15.5 | 0.32 |
| 1199 | 136.8 | 13.68 | 0.33 |

Fig. 1. Schematic of the principle and the implementation for MTC treatment. Schematic of a the MTC principle, b the generation of force and heat during MTC, and c the experimental device for MTC treatment

Fig. 2. Microstructure of Inconel 718. a The grain color map of Inconel 718. b The grain size distribution of Inconel 718

Fig. 3. Chemical composition of Inconel 718

Fig. 4. Schematic of the displacement of the mechanical ultrasonic vibration tool

Fig. 5. The model of FEM simulation

Fig. 6. Ultra-precision machining of Inconel 718

Fig. 7. Microstructure of the treated Inconel 718 with different peak currents during MTC treatment. a TEM bright-field image of the treated top surface with 0 A. b Metallograph of the treated section with an optical magnification of × 200 with 0 A. c TEM bright-field image of the treated top surface with 600 A. d Metallograph of the treated section with an optical magnification of × 200 with 600 A. e TEM bright-field image of the treated top surface with 1000 A. f Metallograph of the treated section with an optical magnification of × 200 with 1000 A

Fig. 8. The microhardness and the average grain size of the treated Inconel 718 surface with different peak currents. A) The microhardness map in the depth of the surface. B) The average grain size of the treated surface

Fig. 9. Numerical simulation results after MTC treatment. Temperature field at the touch point with the peak currents of a) 1000 A, c) 600 A, and e) 0 A, respectively. Equivalent stress field at the touch point with the peak currents of b) 1000 A, d) 600 A, and f) 0 A, respectively

Fig. 10. TEM bright-field image showing the dislocation wall in the treated surface after MTC treatment with the peak current of 1000 A (the arrow points to the dislocation wall)

Fig. 11. XRD pattern of the workpiece surface treated with different peak currents. a) Matrix. b) 0 A. c) 600 A. d) 1000 A

Fig. 12. The pole figure of the Inconel 718 section from the top surface of 70 μm treated with different peak currents. a) Matrix. b) 0 A. c) 600 A. d) 1000 A

Fig. 13 Surface topography of machined Inconel 718 treated with different peak currents. a) Matrix. b) 0 A. c) 600 A. d) 1000 A

Fig. 14 Cutting force during ultra-precision machining of Inconel 718 treated with different peak currents

Fig. 15 The model of cutting forces

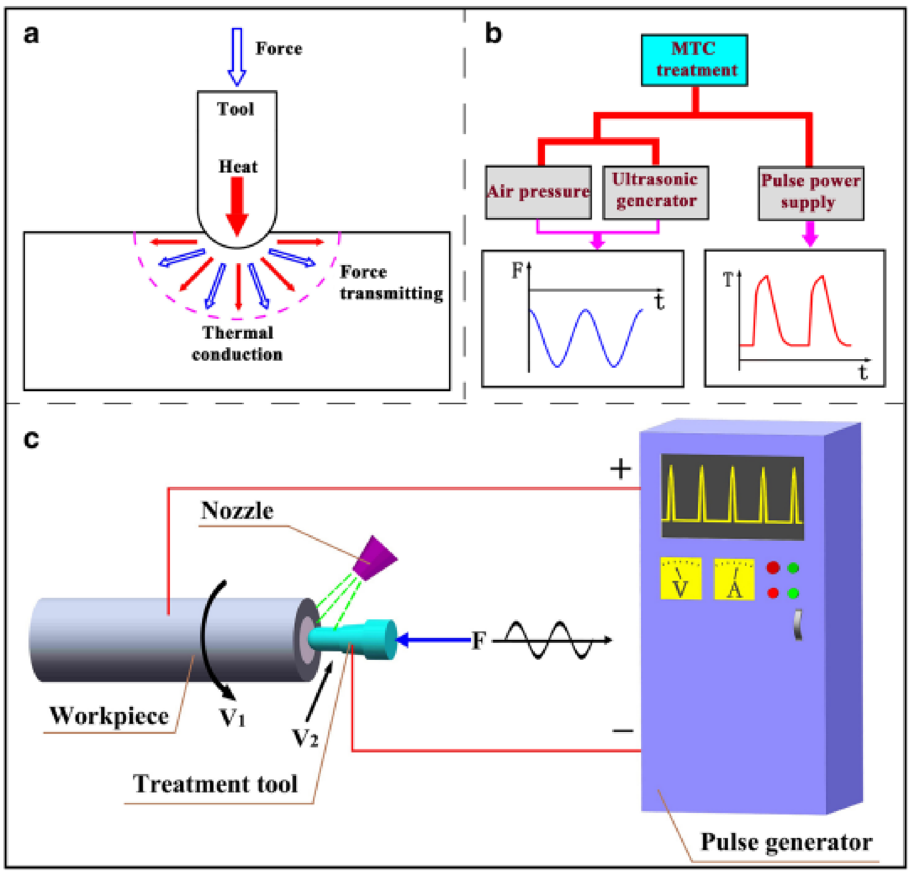

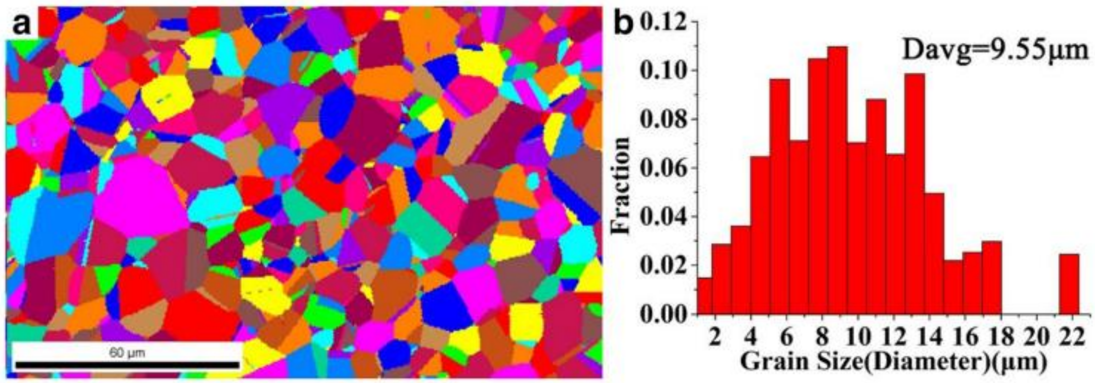
a
60 μm
b
Davg=9.55μm
Fraction
0.12
0.10
0.08
0.06
0.04
0.02
0.00
2 4 6 8 10 12 14 16 18 20 22
Grain Size(Diameter)(μm)

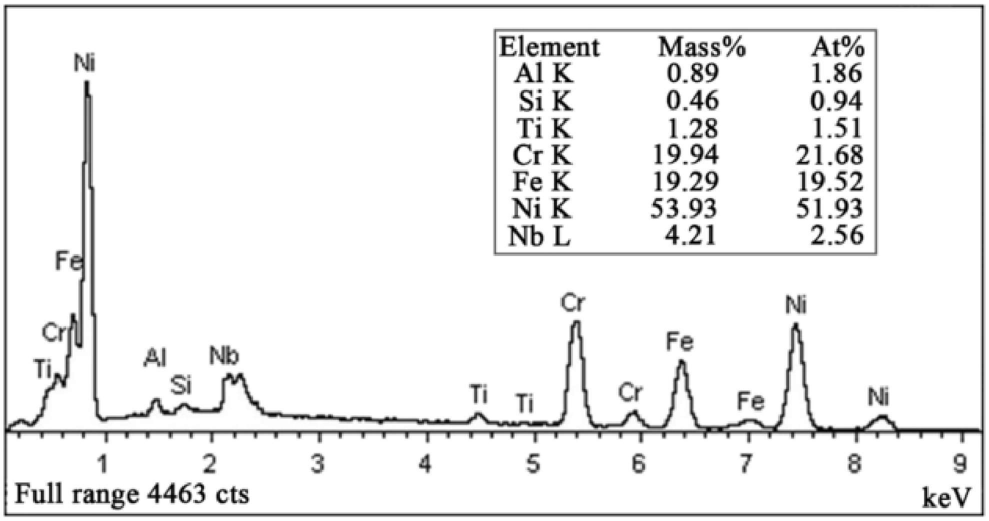
Element Mass% At%
Al K 0.89 1.86
Si K 0.46 0.94
Ti K 1.28 1.51
Cr K 19.94 21.68
Fe K 19.29 19.52
Ni K 53.93 51.93
Nb L 4.21 2.56
Ni
Fe
Cr
Ti
Al
Si
Nb
Ti
Ti
Cr
Cr
Fe
Fe
Ni
Ni
1
2
3
4
5
6
7
8
9
Full range 4463 cts
keV

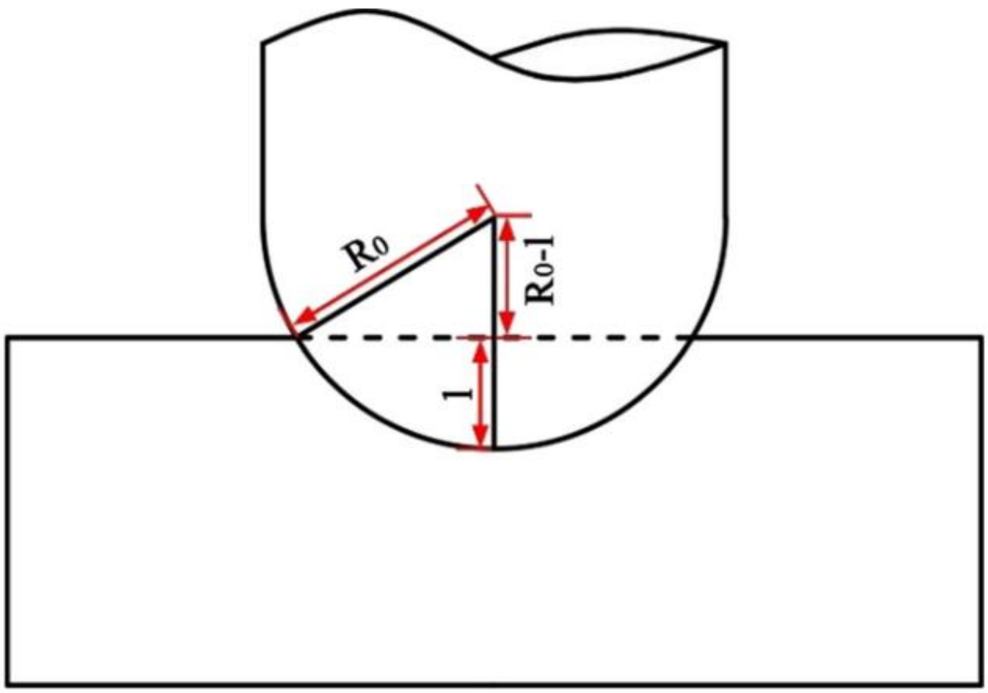
R0
R0-l
l

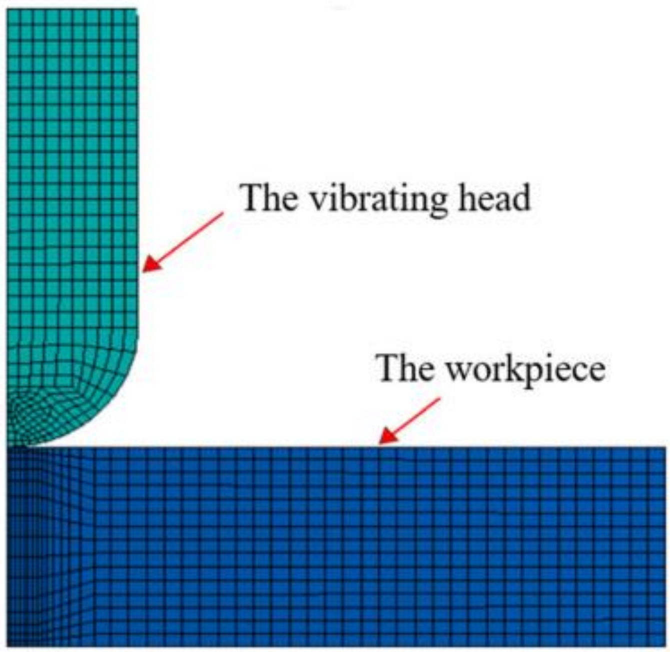
The vibrating head
The workpiece

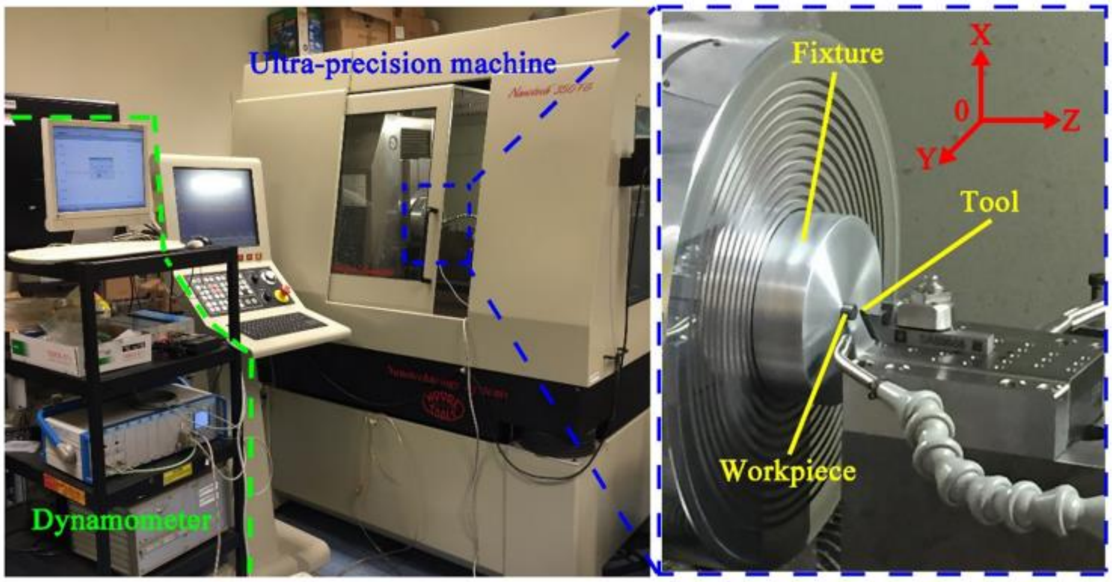
Ultra-precision machine
Dynamometer
Fixture
X
0
Z
Y
Tool
Workpiece

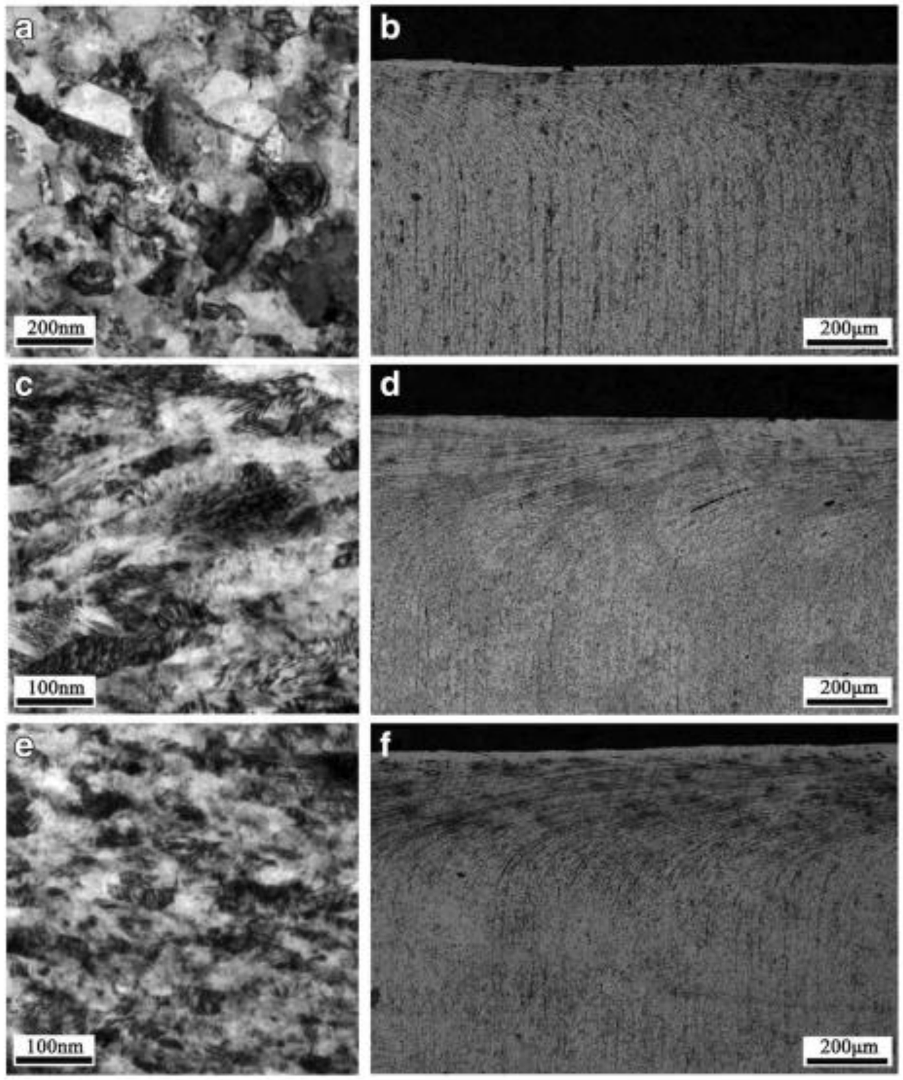
a
200nm
b
200μm
c
100nm
d
200μm
e
100nm
f
200μm

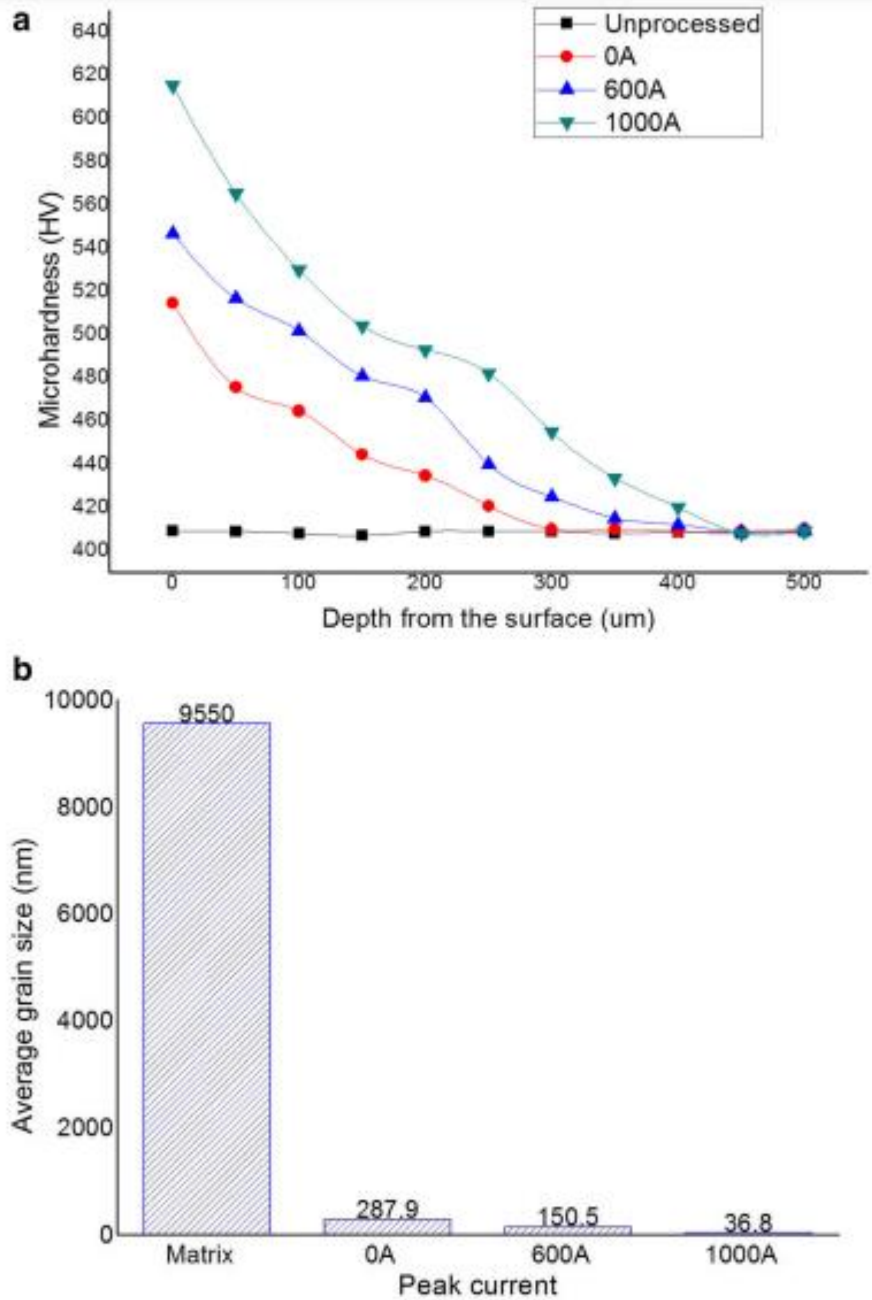

a
Unprocessed
0A
600A
1000A
Microhardness (HV)
640
620
600
580
560
540
520
500
480
460
440
420
400
0
100
200
300
400
500
Depth from the surface (um)
b
Average grain size (nm)
10000
8000
6000
4000
2000
0
9550
287.9
150.5
36.8
Matrix
0A
600A
1000A
Peak current

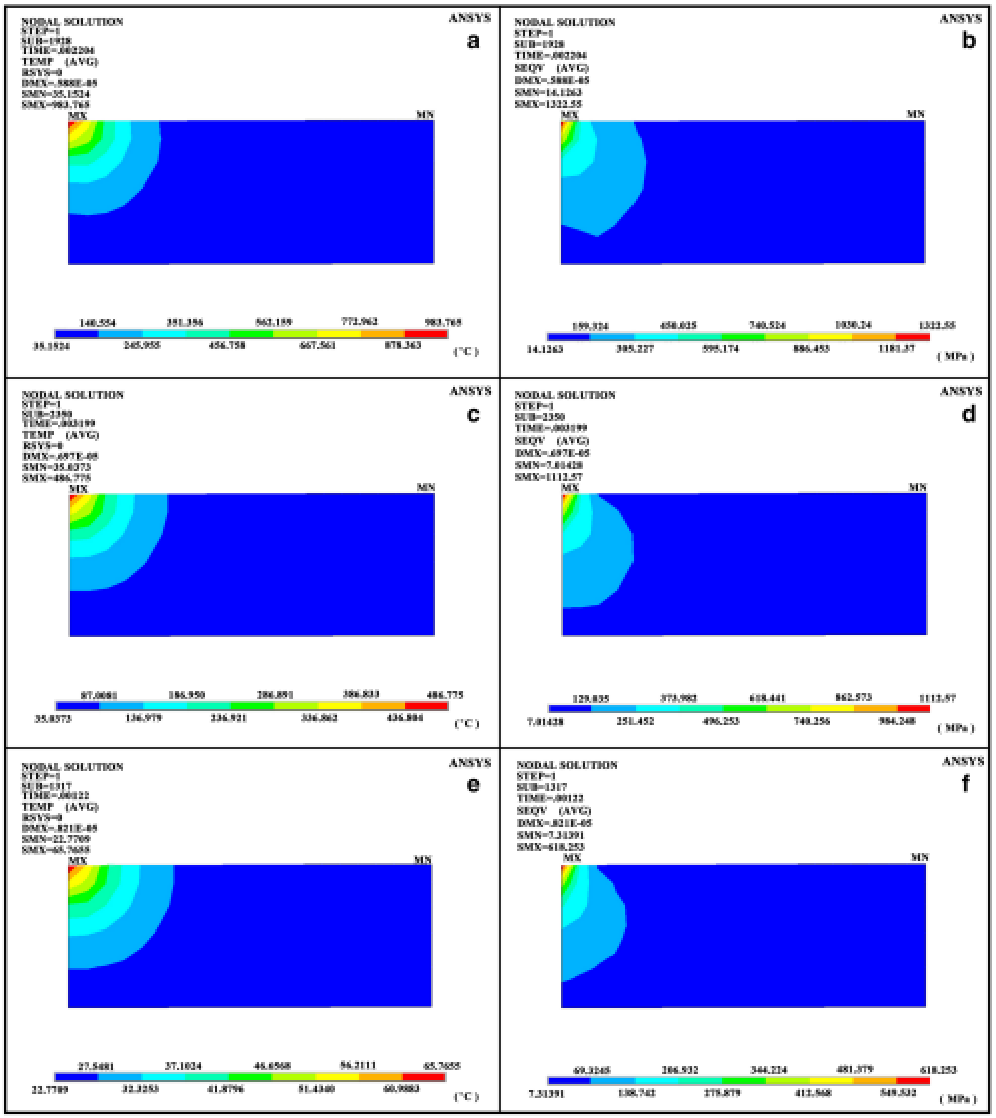
NODAL SOLUTION
STEP=1
SUB=1928
TIME=.002204
TEMP (AVG)
RSYS=0
DMX=.588E-05
SMN=35.1524
SMX=983.765
ANSYS
a
MX
MN
140.554
351.356
562.159
772.962
983.765
35.1524
245.955
456.758
667.561
878.363
(°C)
NODAL SOLUTION
STEP=1
SUB=1928
TIME=.002204
SEQV (AVG)
DMX=.588E-05
SMN=14.1263
SMX=1322.55
ANSYS
b
MX
MN
159.324
450.025
740.524
1030.24
1322.55
14.1263
305.227
595.174
886.453
1181.37
(MPa)
NODAL SOLUTION
STEP=1
SUB=2350
TIME=.003199
TEMP (AVG)
RSYS=0
DMX=.697E-05
SMN=35.0373
SMX=486.775
ANSYS
c
MX
MN
87.0081
186.950
286.891
386.833
486.775
35.0373
136.979
236.921
336.862
436.804
(°C)
NODAL SOLUTION
STEP=1
SUB=2350
TIME=.003199
SEQV (AVG)
DMX=.697E-05
SMN=7.01428
SMX=1112.57
ANSYS
d
MX
MN
129.835
373.982
618.441
862.573
1112.57
7.01428
251.452
496.253
740.256
984.248
(MPa)
NODAL SOLUTION
STEP=1
SUB=1317
TIME=.00122
TEMP (AVG)
RSYS=0
DMX=.821E-05
SMN=22.7709
SMX=65.7655
ANSYS
e
MX
MN
27.5481
37.1024
46.6568
56.2111
65.7655
22.7709
32.3253
41.8796
51.4340
60.9883
(°C)
NODAL SOLUTION
STEP=1
SUB=1317
TIME=.00122
SEQV (AVG)
DMX=.821E-05
SMN=7.31391
SMX=618.253
ANSYS
f
MX
MN
69.3245
206.932
344.224
481.379
618.253
7.31391
138.742
275.879
412.568
549.532
(MPa)

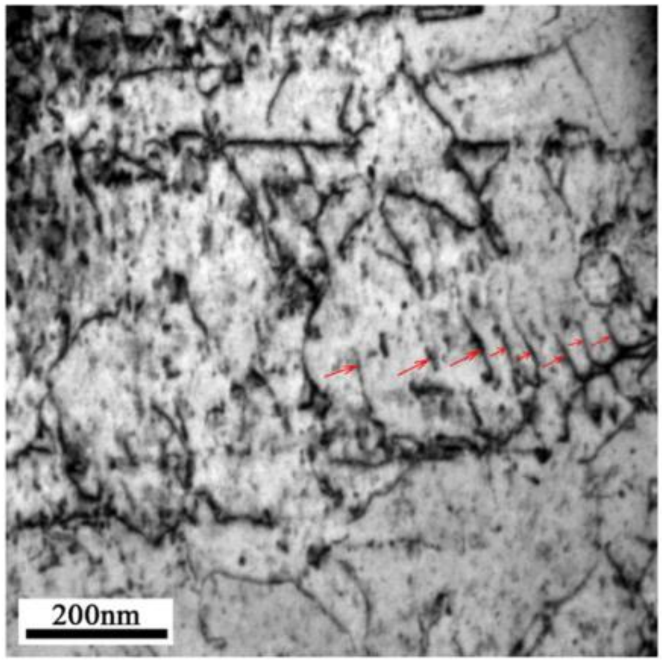
200nm

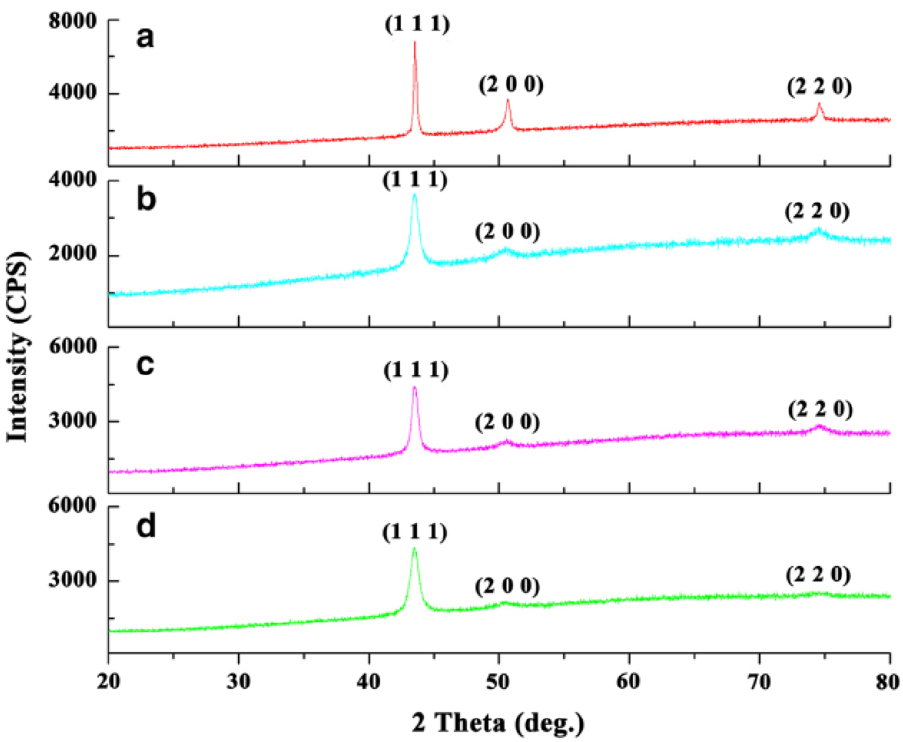
Intensity (CPS)
2 Theta (deg.)
a
(1 1 1)
(2 0 0)
(2 2 0)
b
(1 1 1)
(2 0 0)
(2 2 0)
c
(1 1 1)
(2 0 0)
(2 2 0)
d
(1 1 1)
(2 0 0)
(2 2 0)
8000
4000
4000
2000
6000
3000
6000
3000
20
30
40
50
60
70
80

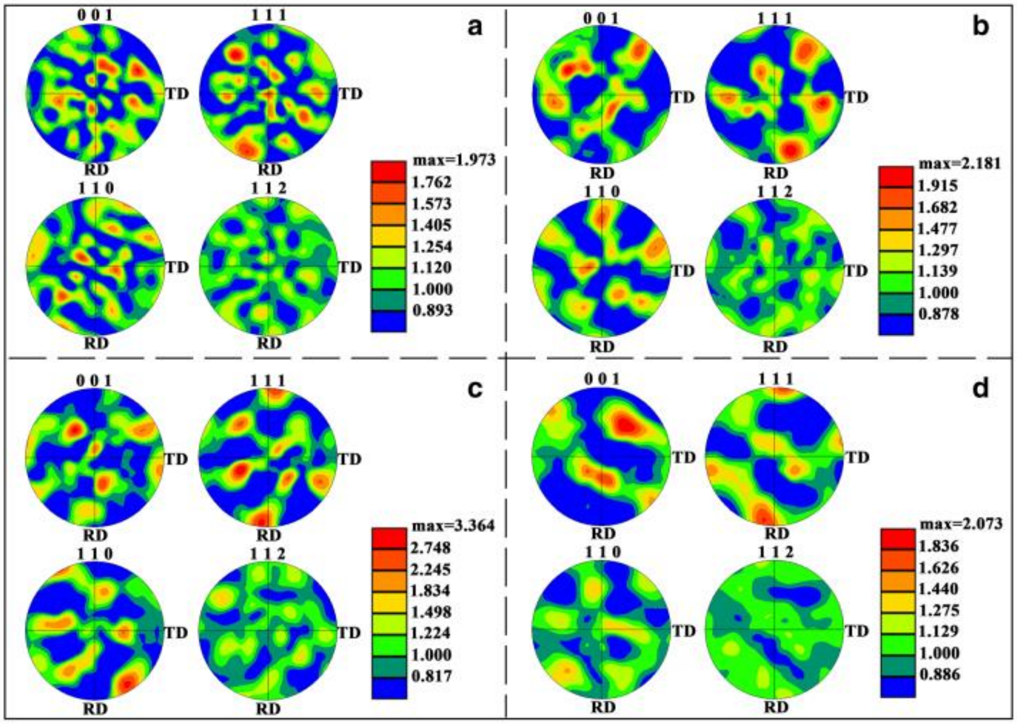
a
0 0 1
1 1 1
1 1 0
1 1 2
TD
RD
max=1.973
1.762
1.573
1.405
1.254
1.120
1.000
0.893
b
max=2.181
1.915
1.682
1.477
1.297
1.139
1.000
0.878
c
max=3.364
2.748
2.245
1.834
1.498
1.224
1.000
0.817
d
max=2.073
1.836
1.626
1.440
1.275
1.129
1.000
0.886

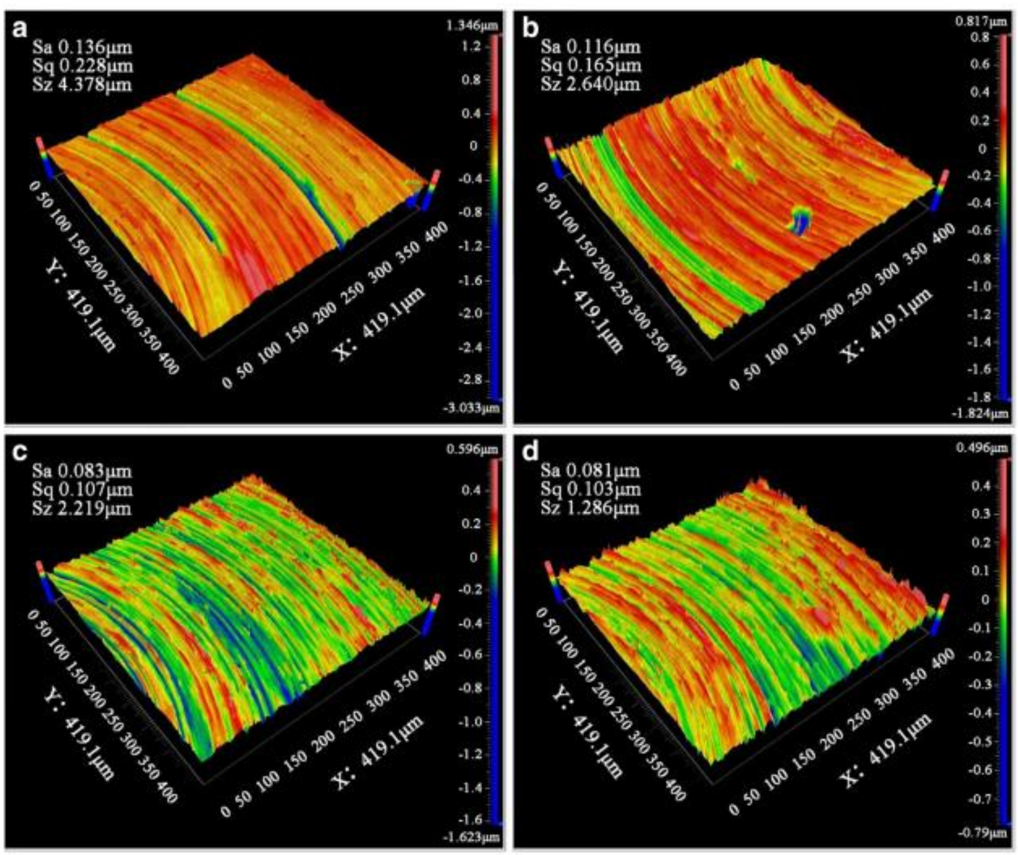
a
Sa 0.136μm
Sq 0.228μm
Sz 4.378μm
1.346μm
-3.033μm
Y: 419.1μm
X: 419.1μm
b
Sa 0.116μm
Sq 0.165μm
Sz 2.640μm
0.817μm
-1.824μm
Y: 419.1μm
X: 419.1μm
c
Sa 0.083μm
Sq 0.107μm
Sz 2.219μm
0.596μm
-1.623μm
Y: 419.1μm
X: 419.1μm
d
Sa 0.081μm
Sq 0.103μm
Sz 1.286μm
0.496μm
-0.79μm
Y: 419.1μm
X: 419.1μm

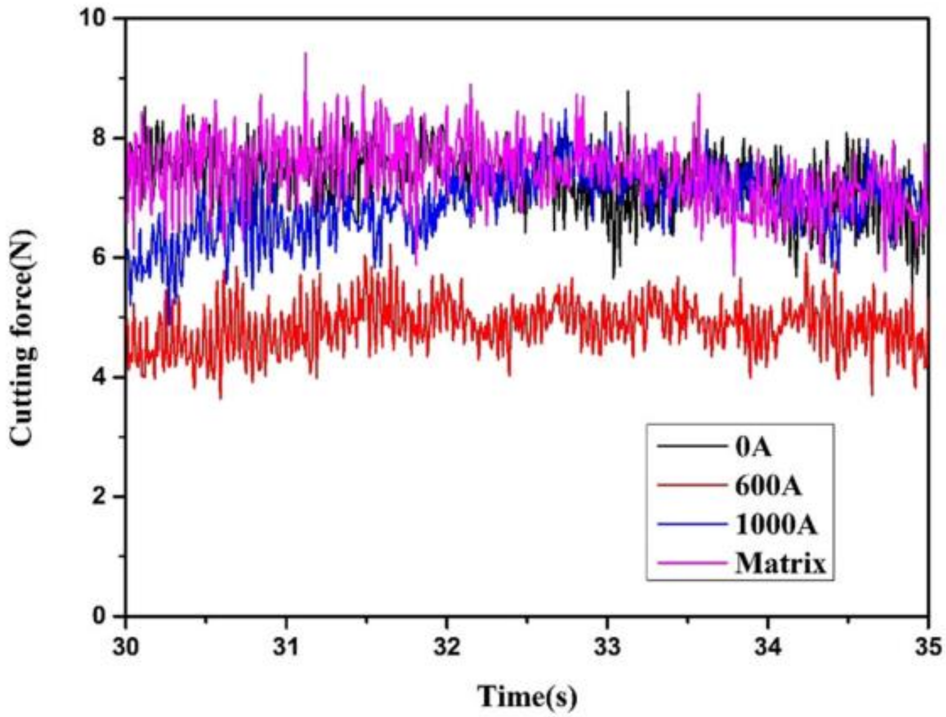

Cutting force(N)
Time(s)
0A
600A
1000A
Matrix
0
2
4
6
8
10
30
31
32
33
34
35


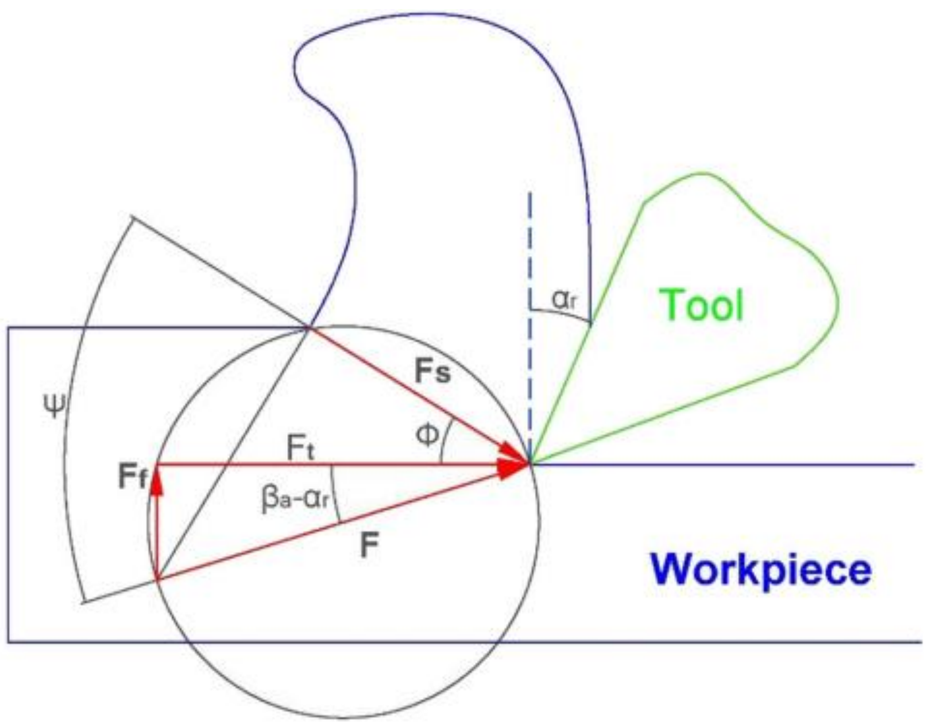

Tool
Workpiece
Fs
Ft
Ff
F
Φ
ψ
αr
βa-αr